# Chapter 8
# Coherent Microscopy and Optical Coherence Tomography for Biomedical Applications

**Jeremy M. Coupland and Justin A.T. Halls**

**Abstract** In recent years the traditional, incoherent methods of optical microscopy have been complemented by coherent imaging methods such as digital holographic microscopy and optical coherence tomography. These methods have the ability to image through distorting media, offer extended contrast enhancement modes such as polarization sensitive and Doppler imaging, and promise varying degrees of 3D imaging capability. Although these techniques might seem quite disparate both in configuration and application, they are similar in many important respects. As coherent, far-field techniques they derive information from the response of the object to a set of optical stimuli and use interferometric methods to record the phase and the amplitude of the elastically scattered field at a distant boundary. Hence, it is only the characteristics of the fields used to illuminate the object and the physical limitations imposed by the optical systems used to measure the response that differentiate the various techniques.

In this chapter, the capabilities of coherent microscopy and optical tomography are compared using linear systems theory. The techniques are characterized in terms of their 3D transfer functions in the frequency domain and their associated 3D point spread functions in the space domain. It is shown that digital holographic techniques that reconstruct images from a single, coherent recording of the scattered field only provide useful 3D information when used to investigate sparse objects such as cells or particles suspended in a transparent fluid. By synthesizing images from multiple recordings of the scattered field using different wavelengths and/or different illuminating wave fronts, the 3D imaging capability of far-field

J.M. Coupland (✉)
Department of Mechanical and Manufacturing Engineering, Wolfson School of Mechanical and Manufacturing Engineering, Loughborough University, Ashby Road, Loughborough, Leicestershire LE11 3TU, UK
e-mail: j.m.coupland@lboro.ac.uk

J.A.T. Halls
Brunel Institute for Bioengineering, Brunel University, Uxbridge, Middlesex UB8 3PH, UK
e-mail: justin.halls@brunel.ac.uk

M.W. Collins and C.S. König (eds.), *Micro and Nano Flow Systems for Bioanalysis*, Bioanalysis 2, DOI 10.1007/978-1-4614-4376-6_8,

optical techniques is extended greatly. In these cases light scattered from different depths can be identified by means of the so-called "coherence gating" or "confocal gating" effects attributed to the source bandwidth and numerical aperture (NA), respectively. These are the methods of optical tomography.

## 8.1 Introduction

Driven mainly by biomedical applications the optical microscope has been in constant development for over a century. Significant milestones include the imaging theory of Abbe [1], the phase contrast technique introduced by Zernike [2, 3], and the confocal microscope by Minsky [4], which for the first time demonstrated 3D sectioned images. More recently we have witnessed the development of digital holographic microscopy (DHM) and other coherent techniques that have similar 3D capability. In particular, Optical Coherence Tomography (OCT) has produced truly remarkable 3D images of the retina and Doppler OCT has been used to estimate blood flow within tissue [5].

Coherent methods differ from their incoherent counterparts by their ability to record and reconstruct both the phase and amplitude of the scattered field, and for this purpose an interferometer is necessary. Of the 3D imaging methods DHM is the fastest and most straightforward to implement. The simplest set-up uses a point-source in an in-line transmission configuration [6] but many variations are possible including phase stepping, off-axis and backscatter geometries [7–9]. In all these cases the definitive characteristic of DHM is that the 3D scattered field can be estimated from a *single measurement of the scattered field*. In biomedical applications DHM can be used to provide bright field images comparable to those from a conventional microscope even when the image is acquired through a distorting sample container such as a plastic dish. It is also possible to emulate other classical microscopy modes such as dark field, differential interference contrast, and phase and even spiral phase contrast [10, 11]. A comprehensive review of DHM techniques has been published by Ferraro, Wax, and Zelevsky in 2010 [12].

As we explain later, DHM does not provide a true 3D image. This is apparent when it is considered that the 3D field is reconstructed from a measurement of a 2D boundary field and as such the reconstruction must be highly correlated. In the strictest sense, a 3D image can only be synthesized from a sequence of scattered field measurements using multiple source wavelengths, illumination directions or a combination of both.

OCT makes use of a broadband or swept source to measure the response of the object *to light of different wavelengths*. Several variants of the technique are possible but all necessarily collect backscattered light from the object of interest. Early OCT measurements exploited a broadband source with limited coherence to record interference as the object was scanned in the object path of an interferometer [13]. The limited coherence results in a packet of interference fringes that identifies

when the path lengths are balanced and provides a so-called "coherence gate" [14]. In the biomedical field this approach is called time-domain OCT (TD-OCT), although the same approach has been used for many years in optical profilometry where it is most often called Coherence Scanning Interferometry (CSI) [15].

Frequency domain OCT (FD-OCT) obviates the need for mechanical scanning. It offers significantly higher data rates and has found widespread application in ophthalmology where it is routinely used to diagnose retinal disorders. FD-OCT can be implemented using either a swept source (typically a semiconductor laser) or a broad-band source (SLED) together with a multiple-channel spectrometer [16]. In either case, FD-OCT measures the phase and amplitude of the scattered signal as a function of wave number. As we explain later, this signal is directly proportional to the amplitude of individual *spatial frequency components* within the object. Many variations of OCT have been developed including Doppler OCT for flow measurement, polarization-sensitive and spectrally resolved OCT [16]. There are several good introductory sources to this rapidly developing field including, Bouma and Tearney [17] and Drexler and Fujimoto [18]. Brezinski [19] also provides a very accessible introduction to the mathematics and basic principles underlying the technique.

An alternative strategy to 3D imaging is to measure the coherent response of an object *to illumination presented from different directions*. Generally known as Optical Diffraction Tomography (ODT) this approach can be implemented in a similar configuration to DHM using scanning mirrors to provide the necessary illumination conditions. In comparison with OCT, ODT can be used in a forward scatter geometry and biomedical applications include quantitative 3D imaging of refractive index in live cells [20]. It is interesting to note that the mutually aligned laser/pinhole combination of a confocal microscope provides an entirely equivalent image to ODT [21]. Confocal microscopy, however, requires 3D scanning of a single point detector, while ODT exploits a 2D scanning mirror and an area detector. More fundamentally, both ODT and confocal microscopy require illumination and observation optics of high numerical aperture (NA) and depth discrimination by this means is often referred to as a "confocal gate" [18]. The basis of ODT in the context of other tomographic techniques is discussed by Kak and Slaney [22], while confocal microscopy and its implementation is treated by Wilson et al. [23].

The pioneering work of Abbe firmly established the link between the NA and the spatial frequency components which are transmitted by a microscope objective and ultimately define the fidelity of the image. In order to increase the lateral resolution, a large NA is required and consequently the highest resolution 3D imaging microscopes must necessarily exhibit a degree of confocal gating even if coherent recording at multiple wavelengths and coherence gating is also exploited. An example of this is CSI. When implemented using low magnification, small NA objectives, coherence gating dominates and the process is entirely equivalent to TD-OCT. If high magnification, large NA objectives are used, confocal gating dominates and the process is entirely equivalent to laser confocal microscopy. Further information on the principles and practice of CSI is to be found in Leach [24].

It is clear from the above discussions that although 3D microscopy techniques might seem quite disparate both in configuration and application, they are similar in many important respects. With the exception of fluorescent confocal microscopy, elastically scattered light is collected from the object of interest and interferometric methods are used to record the phase and the amplitude of the scattered field. In an abstract sense, all optical techniques derive information from the response of the object to a set of optical stimuli with known spatial and temporal characteristics. Hence, it is only the scanning methods that provide the illuminating fields and those used to record the corresponding responses, which differentiate the various techniques.

In previous papers [21, 25] we have applied scalar diffraction theory to many optical imaging techniques, characterizing them as 3D linear systems. In addition we have also considered image enhancing methods such as phase contrast etc. as 3D linear filtering operations [11]. Although the details of this analysis are beyond the scope of the present chapter, the main results provide a useful insight into their capability. In the following sections the basis of linear imaging theory is presented and the theoretical performance of coherent microscopy and optical tomography is then compared.

## 8.2 Linear Imaging Theory

The foundations of 3D linear imaging theory were laid by Wolf [26] and Dandliker [27] who considered the reconstruction of the 3D form of an object from holographic recordings. The theory rests on the assumption of weak scattering or the Born approximation [28]. In effect it is assumed that the scattered field is a small perturbation to the field that illuminates the object. This is often the case in flow measurements, for example, where the fluid is usually sparsely seeded with small tracer particles. Although the Born approximation is not strictly justified in dense tissue, linear theory still provides a good estimate of imaging performance as multiple scattering typically raises noise levels in this situation.

According to linear systems theory [21], the process of imaging can be thought of as a filtering operation that is characterized in the space domain by the 3D convolution integral,

$$O(\mathbf{r}) = \int_{-\infty}^{+\infty} H(\mathbf{r} - \mathbf{r}')\ \Delta(\mathbf{r}')\mathrm{d}^3\mathbf{r}' \tag{8.1}$$

where $H(\mathbf{r})$ is the point spread function (PSF) and $\mathrm{d}^3r = \mathrm{d}r'_x\,\mathrm{d}'r_y\,\mathrm{d}'r_z$. The function $\Delta(\mathbf{r})$ represents the object and in this chapter is defined as the refractive index contrast given by,

$$\Delta(\mathbf{r}) = 4\pi^2(1 - n(\mathbf{r})) \tag{8.2}$$

where, $n(\mathbf{r})$ is the refractive index. The PSF can be thought of as the image of an idealized point scattering particle and its size effectively defines the resolution of the system.

In many ways it is more intuitive to characterize the response of optical systems in the spatial frequency domain ($k$-space or inverse-space) and then go on to calculate the corresponding PSF if required. In this case the transfer function (TF) describes how the individual spatial frequency components that make up the object function are modified by the imaging process. In the frequency domain the 3D convolution of (8.1) can be written, more simply, as the product,

$$\tilde{O}(\mathbf{k}) = \tilde{H}(\mathbf{k})\tilde{\Delta}(\mathbf{k}) \tag{8.3}$$

where tilde represents Fourier transformation such that, $\tilde{H}(k)$, the system TF, is defined as,

$$\tilde{H}(\mathbf{k}) = \int_{-\infty}^{+\infty} H(\mathbf{r}) \exp(2\pi \mathbf{j}\mathbf{k} \cdot \mathbf{r}) \mathrm{d}^3 r \tag{8.4}$$

In the spatial frequency domain it is noted that each point represents a 3D periodic structure or Bragg grating within the object [29]. The 3D structure of a Bragg grating makes it reflect selectively according to both the wavelength, $\lambda$, and the angle of incidence. If the incident and reflected waves are represented by the wave vectors $k_\mathrm{i}$ and $\mathbf{k}_\mathrm{r}$ $|\mathbf{k}_\mathrm{i}| = |\mathbf{k}_\mathrm{i}| = k_0 = 1/\lambda$ then the vector representing $\mathbf{k}_\mathrm{g}$ is given by,

$$\mathbf{k}_\mathrm{g} = \mathbf{k}_\mathrm{r} - \mathbf{k}_\mathrm{i} \tag{8.5}$$

The reflection process is illustrated in Fig. 8.1a, while the relationship described by (8.5) is represented schematically by the wave vector diagram in Fig. 8.1b.

Under the assumption of weak scattering it can be shown that the amplitude of the reflected wave is directly proportional to the amplitude of the refractive index contrast variation [26]. Consequently it is possible to measure the amplitude of a particular spatial frequency component by measuring the response of the object to appropriately chosen illumination and observation directions. In practice, however, source availability and restrictions in the possible illumination and observation directions limit the spatial frequency content that can be measured. In the following sections, the main methods used in 3D imaging systems are described and compared in terms of PSF and transfer characteristics and their potential as measurement tools for the study of micro- and nano-flow studies are then discussed.

## 8.3 Digital Holographic Microscopy

Digital Holographic Microscopy (DHM) is the name given to techniques that reconstruct the phase and amplitude of the scattered field from a single, coherent measurement of the light incident on an imaging array. A fundamental requirement

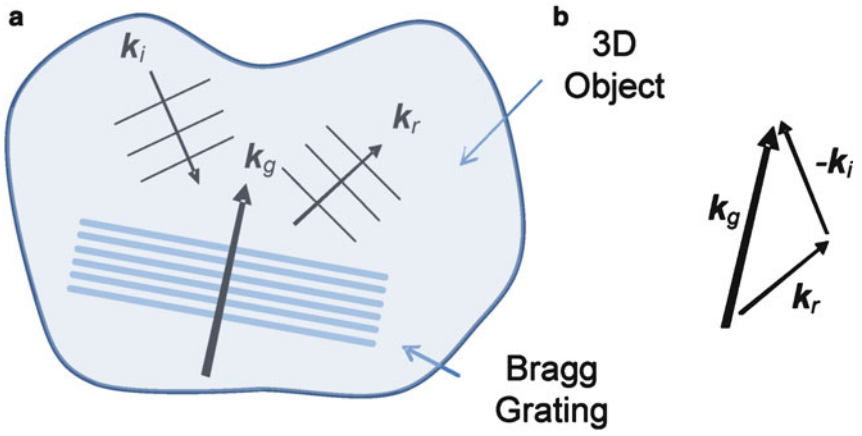


**Fig. 8.1** (**a**) Reflection from Bragg gratings within the object and (**b**) the wave vector diagram

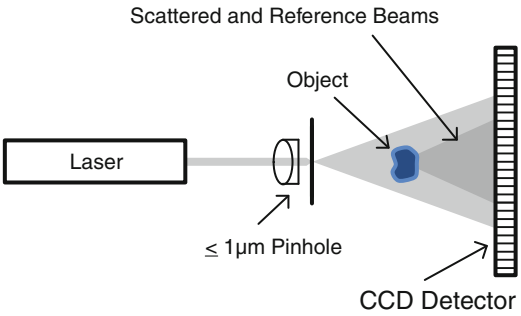


**Fig. 8.2** Point-source, in-line digital holography

of DHM is a coherent reference field which is made to interfere with the scattered field. Provided that the phase and amplitude of the reference field is known, that of the object field can be reconstructed.

Point source in-line holographic microscopy is based on the original idea proposed by Gabor [30, 31] in an effort to get away from the limitations imposed by using physical lenses, and more specifically, the very severe limitations of electromagnetic lenses used in electron microscopy. In the configuration shown in Fig. 8.2, the illumination is provided through a pinhole which is less than a wavelength of light in diameter. The pinhole acts a source of spherical wave fronts that expand as they propagate from the pinhole. The expanding nature of the wave fronts provides magnification. If a CCD detector is illuminated by this wave front it will be uniformly exposed, but if a small scattering object is placed in the field, interference between the direct wave front and the scattered wave fronts is recorded by the CCD.

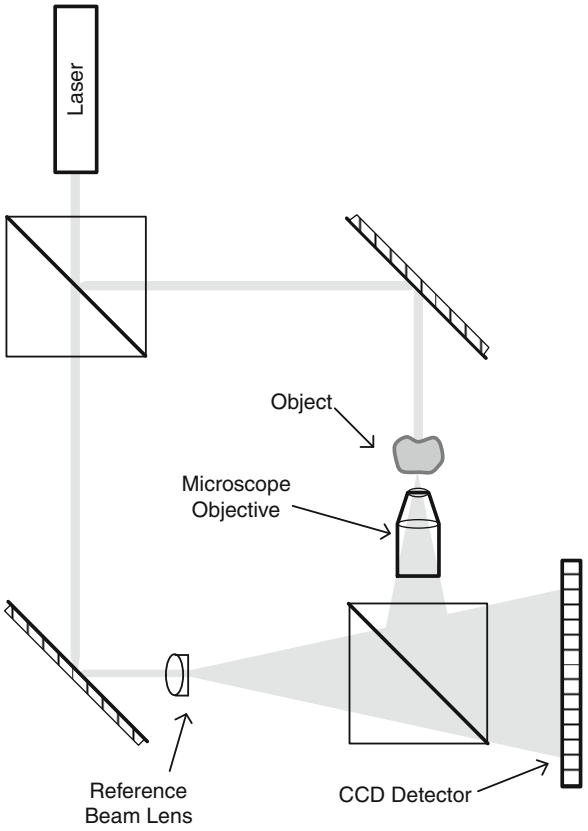


**Fig. 8.3** Forward scatter Mach-Zender interferometric DHM configuration

The simplicity of point-source in-line holography is not without limitations, however. First, restrictions must be placed on the distance between object and pinhole in order that the interference is resolved by the CCD. Second, the assumption that the interference is between scattered and unscattered wave fronts is only reasonable for sparse objects that cover a small fraction of the field as there is strictly no direct path from the pinhole to the detector. Finally, there are many problems associated with numerical reconstruction which must include coordinate transformation and nonlinear optimization methods [32]. The limitations of the in-line holographic method can be overcome either by the off-axis holographic configuration originally proposed by Leith and Upatnieks [33] or phase stepping interferometry [7]. For the purpose of DHM the off-axis geometry has the advantage that the phase and amplitude of the scattered field can be recovered from a single interferogram.

An off-axis transmission DHM based on a Mach-Zender interferometer is shown in Fig. 8.3. In this configuration the microscope objective provides the necessary magnification to ensure that the scattered field is resolved by the CCD. The additional wave front curvature introduced by the objective can be eliminated

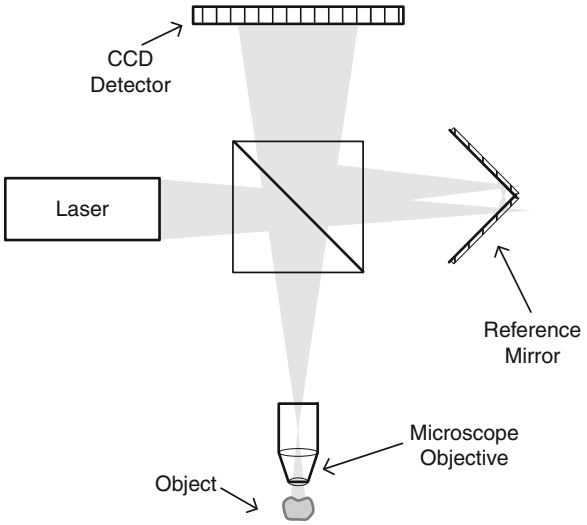


**Fig. 8.4** Backscatter Michelson DHM configuration

by introducing a similar lens into the reference arm of the interferometer. The most important aspect of this configuration is the flexibility to add a tilt (or offset) to the reference wave which introduces a carrier frequency to the interference pattern that simplifies numerical reconstruction considerably.

Off-axis DHM can also be implemented in a reflection geometry using a Michelson interferometer configuration as shown in Fig. 8.4. In this arrangement the laser is focused in the back focal plane of the objective such that the object is illuminated by a plane wave. The light scattered from the object passes back through the objective and forms an image at the CCD. As before, the scattered light is mixed with a coherent reference wave of appropriate divergence and tilt such that plane carrier fringes are observed in the intensity recorded by the CCD.

In general terms, DHM and all the other methods of coherent 3D imaging, measure the scattered field at a boundary surface that is far beyond the reach of the evanescent waves that constitute the near-field that surrounds the object. As a consequence, only plane wave components that have the capability to propagate to the boundary (i.e., the far-field) can be measured in this way. Further to this, it is only the plane wave components that propagate within the NA of the objective, that are collected as shown in Fig. 8.5.

Mathematically, the process of reconstructing the scattered field from this limited information can be written as a linear filtering operation. If in the spatial frequency domain the scattered and reconstructed fields are described by the functions, $\tilde{E}^s(\mathbf{k})$ and $\tilde{E}^m(\mathbf{k})$, the DHM reconstruction process can be written as the product [21],

$$\tilde{E}^m(\mathbf{k}) = \tilde{E}^s(\mathbf{k})\tilde{G}_{\mathrm{NA}}(\mathbf{k}) \tag{8.6}$$

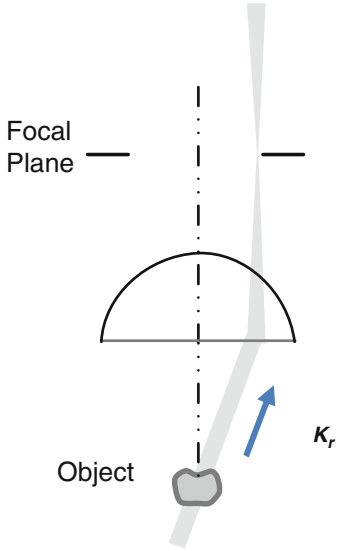


**Fig. 8.5** Coherent microscopy configuration

where $\tilde{G}_{\mathrm{NA}}(\mathbf{k})$ represents the wave vectors collected by the system. For the case of a coherent microscope operating at wavelength, $\lambda$ , the plane wave components collected by the circular aperture can be represented in $k$-space by wave vectors, $\mathbf{k}_{\mathrm{r}}$ that fall on a spherical shell with a radius equal to the wave number $k_0 = 1/\lambda$. Accordingly $\tilde{G}_{\mathrm{NA}}(\mathbf{k})$ is given by,

$$\tilde{G}_{\mathrm{NA}}(\mathbf{k}) = \frac{j}{4\pi k_{\mathrm{o}}}\delta(|\mathbf{k}| - k_0) \cdot \mathrm{step}\left(\frac{\mathbf{k}\cdot\hat{\mathbf{o}}}{k_{\mathrm{o}}} - \sqrt{1 - N_{\mathrm{A}}^2}\right) \tag{8.7}$$

where $N_{\mathrm{A}}$ is the NA of the objective, $\hat{\mathbf{o}}$ is a unit vector in the direction of the viewing axis, and $\delta(x)$ and $\mathrm{step}(x)$ represent the Dirac delta function and Heaviside step function, respectively.

It is clear that (8.3) and (8.6) have identical form; however, it is important to emphasize that the TF, $\tilde{H}(\mathbf{k})$ in (8.3), is applied to the *spectrum of the object function*, $\tilde{\Delta}(\mathbf{k})$, whereas $\tilde{G}_{\mathrm{NA}}(\mathbf{k})$ modifies the *spectrum of the scattered field*, $\tilde{E}^s(\mathbf{k})$. In order to calculate the TF for DHM, $\tilde{H}_{\mathrm{DHM}}(\mathbf{k})$, it is necessary to consider the illumination. From the discussions in Section 2 it is apparent that if the object is illuminated by a plane wave described by the vector $k_{\mathrm{i}}$, $\tilde{H}_{\mathrm{DHM}}(\mathbf{k})$, and $\tilde{G}_{\mathrm{NA}}(\mathbf{k})$ are related such that,

$$\begin{aligned}\tilde{H}_{\mathrm{DHM}}(\mathbf{k}) &= \tilde{G}_{\mathrm{NA}}(\mathbf{k} + \mathbf{k}_{\mathrm{i}}) \\ &= \frac{j}{4\pi k_{\mathrm{o}}}\delta(|\mathbf{k} + \mathbf{k}_{\mathrm{i}}| - k_0) \cdot \mathrm{step}\left(\frac{(\mathbf{k} + \mathbf{k}_{\mathrm{i}})\cdot\hat{\mathbf{o}}}{k_{\mathrm{o}}} - \sqrt{1 - N_{\mathrm{A}}^2}\right)\end{aligned} \tag{8.8}$$

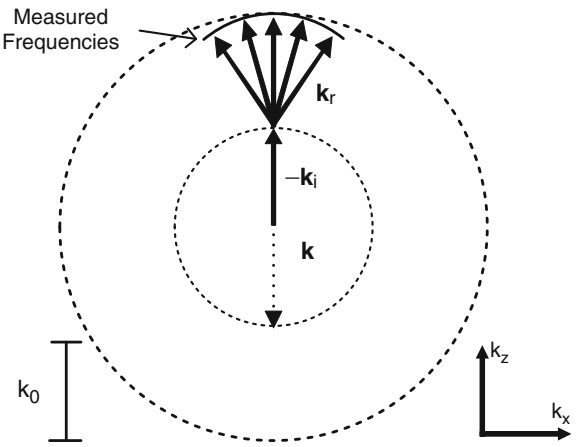


**Fig. 8.6** TF of a coherent microscope

A DHM is therefore sensitive to spatial frequencies within the object function that lie on a spherical shell of radius equal to the wave number that is translated from the origin by a vector equal to $-\mathbf{k}_i$. This is illustrated in Fig. 8.6 for the case of axial backscatter illumination, where $\mathbf{k}_i = -k_0\hat{\mathbf{o}}$.

Inverse Fourier transformation of the TF gives the PSF and provides further insight into the imaging process. This has been computed for a back-scatter DHM configuration with NA $= 0.55$ operating at $\lambda = 600$ nm and a section through this distribution is shown in Fig. 8.7.

By definition the PSF of an instrument provides the image of a weakly scattering point object. For DHM it is found that the intensity of the PSF decreases as the square of the distance in the observation direction from its center, in exactly the same way as a focused beam. This means that the total power in any plane perpendicular to the optical axis remains constant and as such a DHM does not produce a 3D image in the strictest sense [5]. Nevertheless, if it is used to investigate sparsely seeded flows, individual particles can be distinguished as bright points in the reconstruction and their 3D position can be measured [34].

A good example of DHM taken from a study of underwater microbiology by Jorge Garcia-Sucerquia et al. [6] is shown in Fig. 8.8. This image is a reconstruction from an in-line hologram.

## 8.4 Optical Coherence Tomography

Optical Coherence Tomography (OCT) differs fundamentally from DHM because it measures the coherent response of the object *to light of different wavelengths*. Imaging OCT was originally proposed by Huang et al. [13] and has been practiced in many forms. OCT has major applications in opthalmology where it is used extensively to diagnose retinal disorders. For these applications it is convenient to use galvanometer scanning mirrors to scan the retina as shown in the so-called fundus camera illustrated in Fig. 8.9.

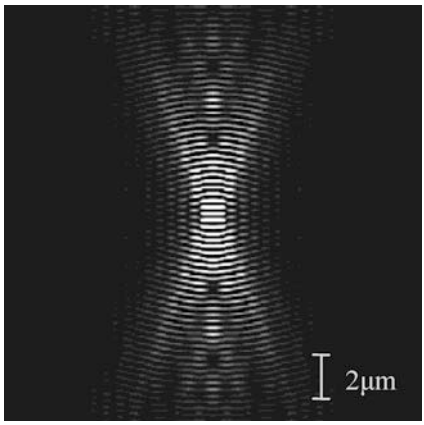


**Fig. 8.7** PSF of a coherent microscope (positive real part shown)

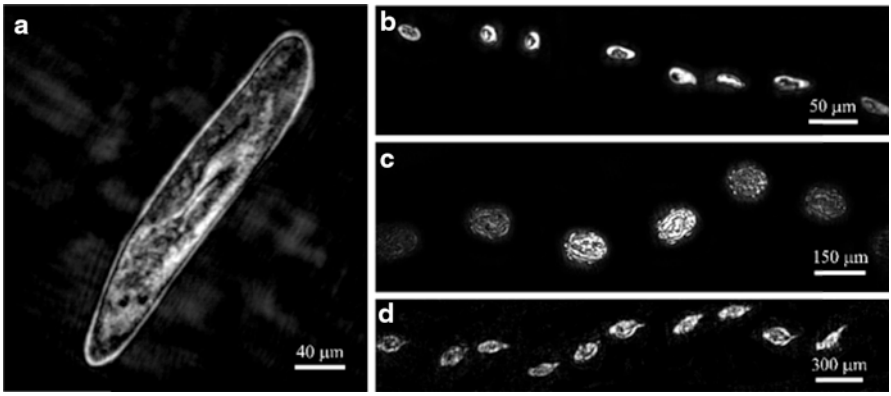


**Fig. 8.8** Images taken with underwater DHM. (**a**) Paramecium. (**b–d**) Trajectories of various species swimming through the observation window, with a frame rate of 10 frames/s. (**b**) Ciliate; (**c**), Didinium; (**d**) Rotifer (Reproduced with permission)

The scanning system is connected to the interferometer or OCT engine unit by a fiber optic. Early time domain ophthalmic OCT systems (TD-OCT) used the Michelson interferometer configuration as shown in Fig. 8.10. In this case the interference between object and reference paths is recorded as the depth scan is performed by a mechanically driven mirror. OCT requires a bright light source of limited temporal coherence and super-luminescent diodes, ultrashort pulse and super-continuum lasers have all been used for this purpose [18].

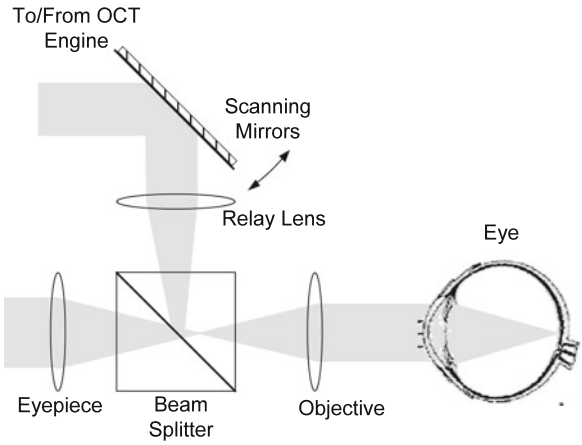


**Fig. 8.9** Fundus camera

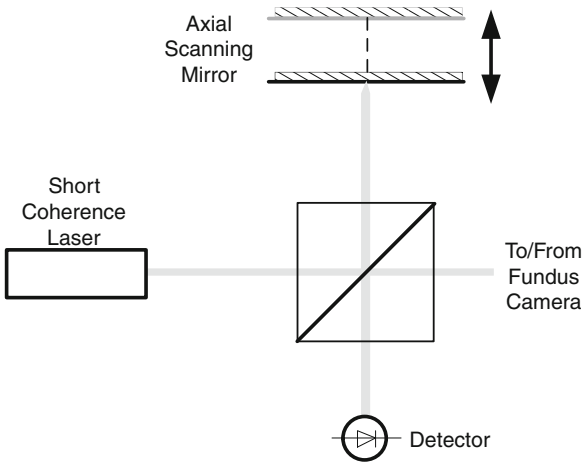


**Fig. 8.10** Time domain OCT

With TD-OCT scanning speeds are generally slow. State-of-the-art systems can achieve scan rates up to 8,000 depth scans/s but the reduced sensitivity at these scanning speeds makes retinal imaging impracticable [18]. The need for mechanical scanning is obviated in frequency domain OCT (FD-OCT) and consequently the time necessary to perform a depth scan can be reduced dramatically.

FD-OCT can be implemented using either a tunable source or a white light source together with a spectrometer array as shown in Fig. 8.11. In either case the interference between object and reference paths is recorded as a function of the source frequency (or wave number). In contrast with TD-OCT, the interference signal acquired by FD-OCT has greater modulation and a significantly greater signal to noise ratio (SNR). For this reason FD-OCT is preferred in high speed, high resolution systems.

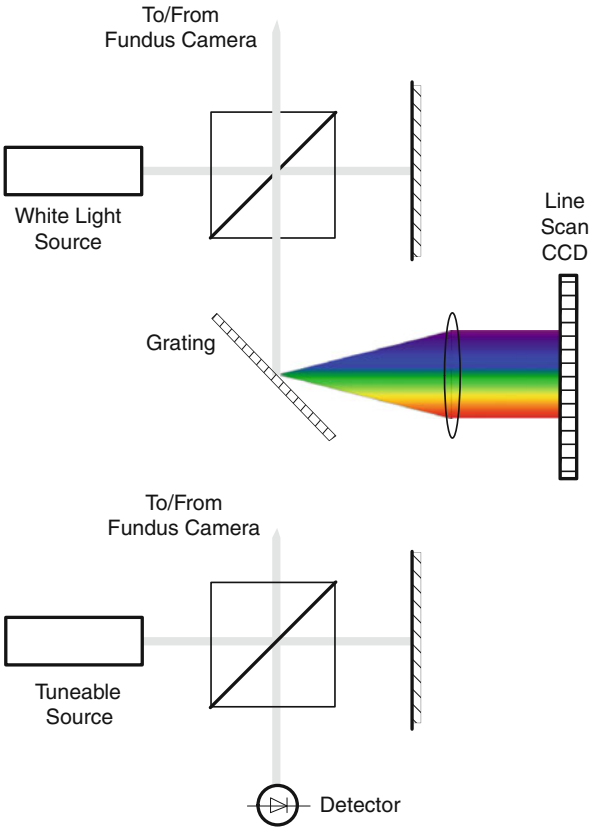


**Fig. 8.11** Frequency domain OCT

Although there are many ways to implement OCT they all measure the coherent response of an object when the *wavelength* of the illumination is varied. An FD-OCT system can be considered as the superposition of images from a coherent microscope made at different wavelengths as shown schematically for illumination with four different wave numbers in Fig. 8.12.

In a practical system the illumination wavelength is scanned and if the frame rate of the detector is sufficient, the measured frequencies form a continuum. In this case the TF of the system can be written as the superposition integral [21],

$$\tilde{H}_{\mathrm{OCT}}(\mathbf{k}) = \frac{j}{4\pi}\int_{-\infty}^{+\infty}\frac{S(k_{\mathrm{o}})}{k_{\mathrm{o}}}\delta(|\mathbf{k}+\mathbf{k}_i|-k_0) \cdot \mathrm{step}\left(\frac{(\mathbf{k}+\mathbf{k}_i)\cdot\hat{\mathbf{o}}}{k_{\mathrm{o}}} - \sqrt{1-N_{\mathrm{A}}^2}\right)\mathrm{d}k_0 \tag{8.9}$$

where $S(k_{\mathrm{o}})$ is the source spectrum expressed as a function of wave number. Inverse Fourier transformation of this expression gives the PSF that is shown in Fig. 8.13. For the sake of comparison, the PSF has been computed for a system with the

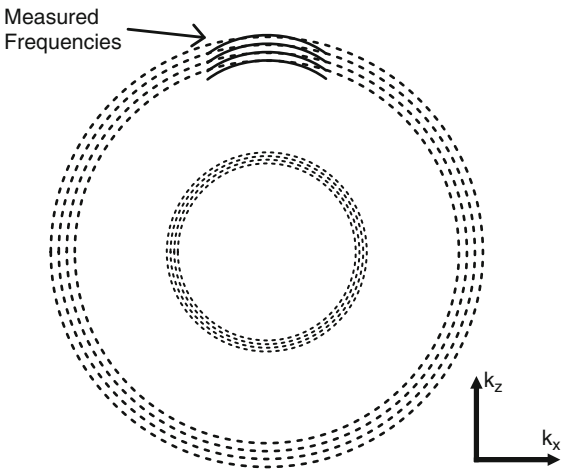


**Fig. 8.12** TF of an OCT system

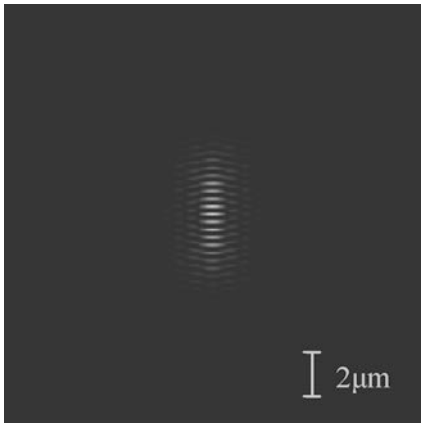


**Fig. 8.13** PSF of an OCT system (positive real part shown)

previous NA = 0.55 operating with the same mean wavelength of $\lambda = 600$ nm and a Gaussian spectral distribution with bandwidth of 100 nm (FWHH@$1/e^2$). It can be seen that in comparison with the PSF of DHM shown in Fig. 8.7, the total intensity of the OCT PSF reduces in planes orthogonal to the viewing direction and OCT therefore provides greatly enhanced 3D information. In OCT the extent of the PSF in the axial (i.e., observation) and lateral (perpendicular to the observation) directions are inversely proportional to the source bandwidth and the NA, respectively. It is important to point out that most commercial OCT systems operate with much reduced aperture (NA = 0.01) resulting in a PSF with proportionately larger lateral dimensions.

Fig. 8.14 provides a good example of OCT in medical imaging taken from an in vivo study of human skin by Alex et al. [35]. Depth sections (B-scans) through the surface clearly identify the different layers up to a depth of around 3 mm.

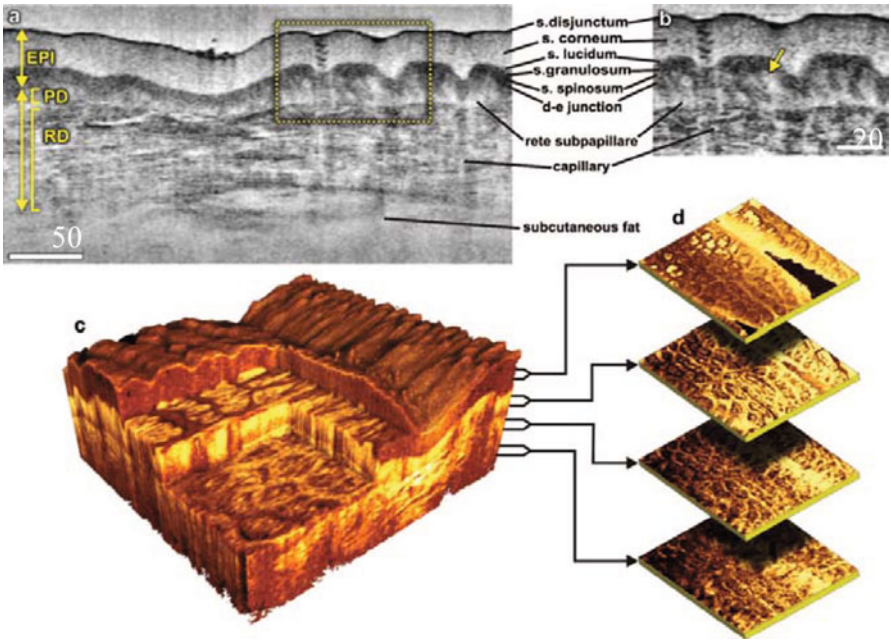


**Fig. 8.14** OCT skin images at 1,300-nm (**a**) B-scan of skin above the proximal interphalangeal joint of the middle finger. (**b**) Magnified view of epidermis and dermis (*yellow arrow* points towards the dermal–epidermal junction). (**c**) 3D rendering of the same region reconstructed using 1024 B-scans. (**d**) En face sections of the same (Reproduced with permission)

## 8.5 Coherence Scanning Interferometry

CSI and confocal microscopy can also be considered to be tomographic techniques and are discussed together in this section because they both provide additional 3D information that is beyond that obtainable using coherent microscopy and OCT. This information is the response of the object to illuminating plane waves *propagating at different angles*. Interestingly, both CSI and confocal microscopy predate coherent microscopy and OCT.

In CSI the object is illuminated by a wide-band distributed source (halogen or LED) through a Mirau interference objective as shown in Fig. 8.15. Interference between the light reflected from a reference surface (within the Mirau objective) and that from the objective is recorded by the CCD as the object is scanned through focus. Considering first the distributed nature of the source, the interference fringes generated by a quasi-monochromatic CSI can be considered to be due to the superposition of coherent recordings made of different plane waves propagating at different angles [21]. The response is illustrated schematically for five different plane wave illuminations in Fig. 8.16.

In practice, if a distributed source and appropriate condenser lenses are used to fill the aperture of the objective, the TF becomes a continuum within the region shown.

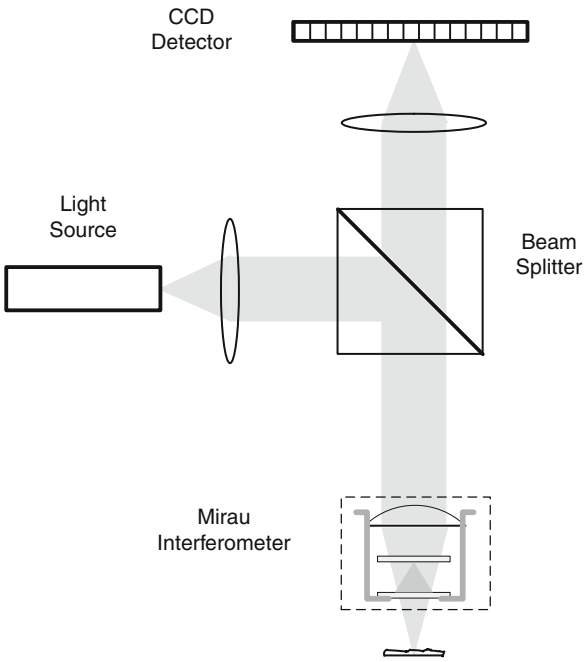


**Fig. 8.15** CSI configuration

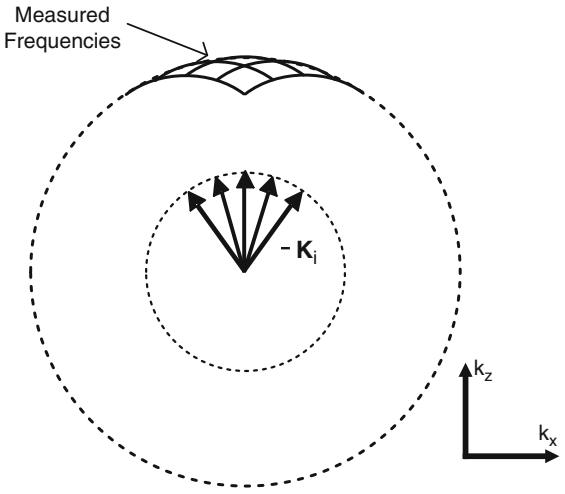


**Fig. 8.16** TF of quasi-monochromatic CSI system

If we now consider a polychromatic source the superposition results in the TF shown schematically in Fig. 8.17. In practice a source will have a smooth spectrum and the TF will be a continuum defined by,

$$\tilde{H}_{\mathrm{CSI}}(\mathbf{k}) = \int_{-\infty}^{+\infty} S(k_0)A(\mathbf{k})\mathrm{d}k_0 \tag{8.10}$$

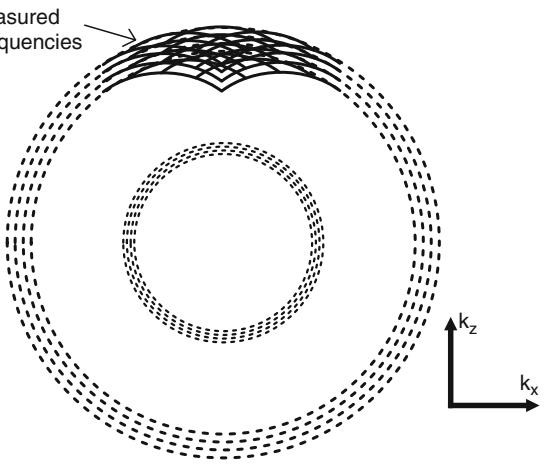


**Fig. 8.17** TF of a polychromatic CSI system

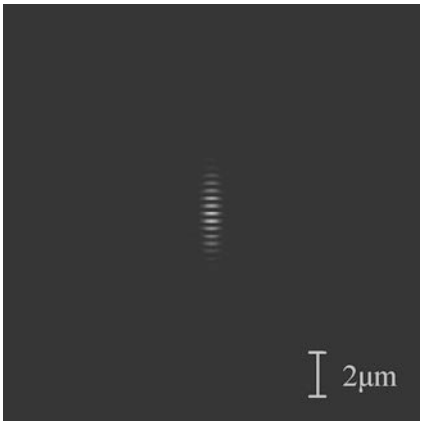


**Fig. 8.18** PSF of a CSI system (positive real part shown)

where the function $A(\mathbf{k})$ is defined by the convolution,

$$A(\mathbf{k}) = \int_{-\infty}^{+\infty} \tilde{G}_{\mathrm{NA}}(\mathbf{k}')\tilde{G}_{\mathrm{NA}}(\mathbf{k}-\mathbf{k}')\mathrm{d}^3k' \tag{8.11}$$

For the sake of comparison, the PSF has been computed in Fig. 8.18 for a CSI with NA = 0.55 operating with the same mean wavelength of $\lambda = 600$ nm and a Gaussian spectral distribution with bandwidth of 100 nm (FWHH@$1/e^2$). It can be seen that the lateral dimensions of the PSF are approximately half that of the coherent microscope and the OCT system (Fig. 8.7 and Fig. 8.13) while the axial extent is slightly reduced.

Interestingly, the PSF of a laser confocal microscope (configuration shown in Fig. 8.19) is directly related to that of CSI [21]. In confocal microscopy, however, the detection process is not usually coherent (i.e., not interferometric) and consequently the PSF takes the form of the envelope of the PSF of a quasi-monochromatic CSI of the same NA.

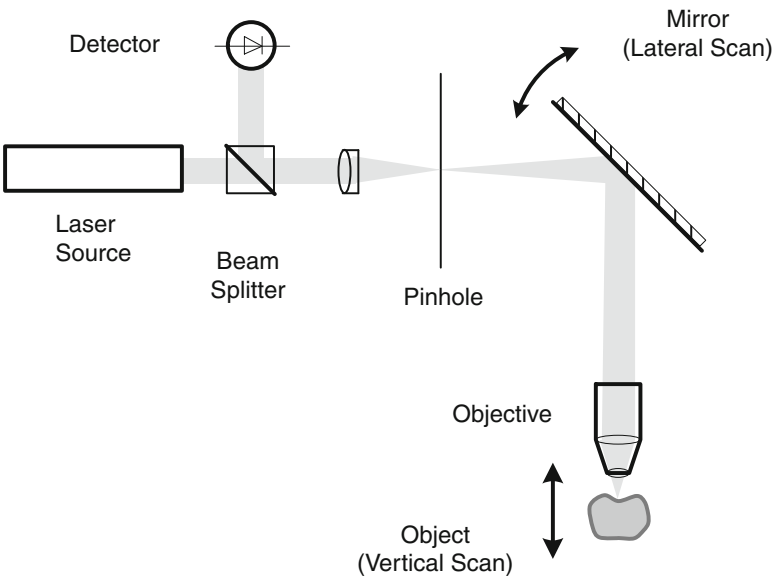


**Fig. 8.19** Confocal microscope

From the discussions above it is clear that CSI and confocal microscopy are able to resolve twice the spatial frequency of OCT or DHM. It is also noted that at low NA the axial extent of the PSF for both CSI and OCT is inversely proportional to the source bandwidth. For quasi-monochromatic CSI and confocal microscopy, however, the axial extent is inversely proportional to the squared NA. For broadband CSI systems the axial extent is either bandwidth or NA limited and for typical systems a crossover is observed when NA $\approx 0.3$.

## 8.6 Imaging Performance

In the previous sections we have introduced the methods of coherent microscopy and optical tomography and have characterized their performance in terms of 3D linear imaging theory. The response of the system to spatial frequencies within the object function, or refractive index contrast, is characterized by the TF which, in turn, depends on the aperture of both the illumination and observation optics. The PSF describes the appearance of a point-like object and is the inverse Fourier transform of the TF. The PSF has been calculated for backscatter DHM, OCT, and CSI configurations of equal NA as it provides a useful way to compare the 3D imaging performance of the techniques.

In all the calculated cases the PSF has a cyclic variation in phase along the central axis with a period approximately equal to half the mean wavelength.

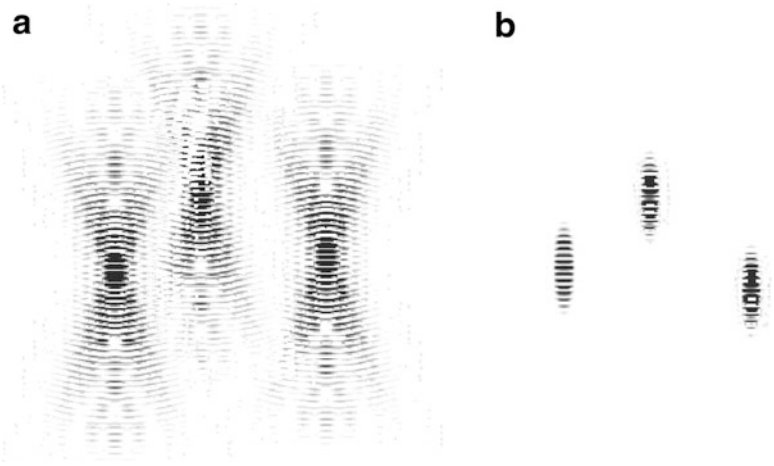


**Fig. 8.20** Images of sparse particles using (**a**) DHM and (**b**) OCT

This is a characteristic of the backscatter geometry. A clear distinction between DHM, which uses a single illumination wave and that of the other tomographic techniques that in effect synthesize images from coherent recordings made with either multiple wavelengths and/or multiple illumination directions, is apparent. For the case of DHM (Fig. 8.7), the axial extent of the PSF is considerably greater than the tomographic techniques (Fig. 8.13 and Fig. 8.18). More precisely it can be shown that the total intensity in any plane perpendicular to the central axis of the PSF is equal. The effect of the PSF depends on the application. DHM has been used to measure fluid flow fields in micro-fluidic devices using the technique known as holographic particle image velocimetry (HPIV) [36]. In this application a transparent fluid is sparsely seeded with small particles and images are recorded at two or more instants in time. Since the PSF is by definition the image of a point object it is clear that provided that the particles are sufficiently small their images will take the form of the PSF. As a particle moves, its reconstructed image will move in sympathy and the particle velocity can be deduced by estimating the displacement of its image using correlation for example.

Using the PSFs previously calculated for the DHM and OCT systems a typical image of a sparsely seeded fluid is illustrated in Fig. 8.20. The effect of the PSF is immediately clear. If the particles are separated sufficiently then their images will be distinguishable and their 3D position can be estimated. If the particles are too close, however, the images will overlap, interfere, and become indistinguishable from a uniform background of laser speckle. Analysis shows that an upper limit on the total number of particles that can be identified in this way is proportional to the number of pixels required to record an optimally sampled holographic image [37]. Additional noise sources reduce this limit, however, and typically around $10^4$ particles/mm$^3$ can be identified in practice.

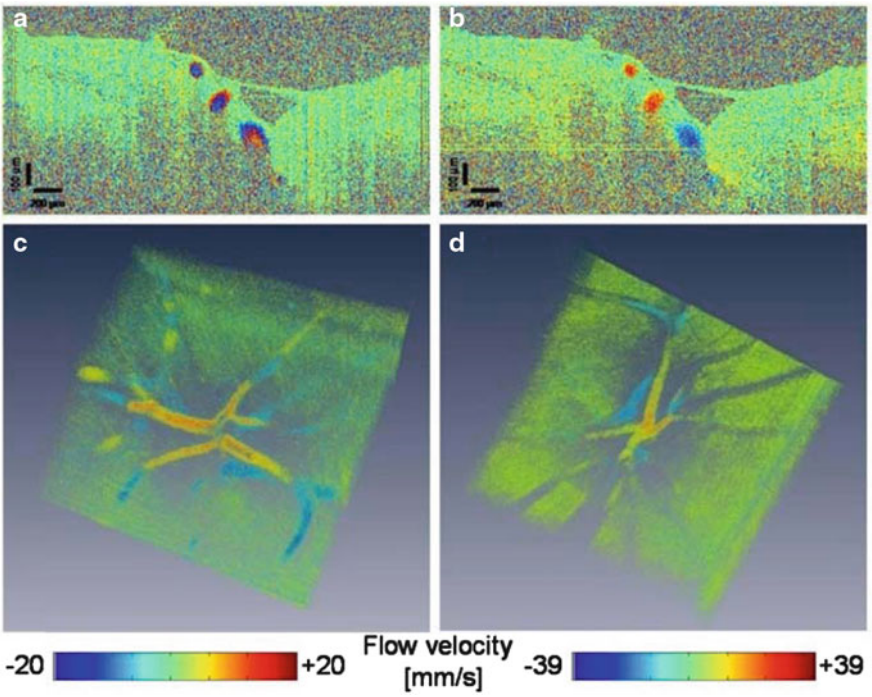


**Fig. 8.21** Volumetric Doppler OCT imaging of retinal vasculature. (**a** and **b**) B-scan images close to the optic disk at 100 kHz and 200 kHz, respectively. (**c** and **d**) volumetric images of the retinal arteries and veins branching in the optic disk at 100 and 200 kHz

The PSFs of OCT, CSI and confocal microscopy reduce much more quickly in the axial direction than those of DHM and consequently many more particles can be distinguished per unit volume. The number of particles that can be distinguished is now inversely proportional to the volume of the PSF. From the dimensions of the OCT PSF shown in Fig. 8.13 we might expect around $10^8$ particles per $mm^3$ while a lower NA OCT system (NA = 0.01) might return $10^4$ particles per $mm^3$.

As mentioned previously, if the number concentration is increased the images of particles will overlap and interfere and the image will take on a speckled appearance. With the tomographic techniques, OCT, CSI, and confocal microscopy, it is possible to identify local changes in number density as the speckle will become proportionately brighter or darker. This is not true for the case of DHM, however; the slow decay of the PSF in the axial direction means that any 3D information is lost. For this reason it is necessary to use a tomographic method to image through tissue. As the number concentration or equivalently the scattering coefficient increases, however, the assumption of weak scattering (the Born approximation) breaks down and the effects of multiple scattering are observed. Typically this increases background noise in the reconstruction as a function of depth but can sometimes lead to a significant shadowing effect in low NA tomographic systems [18].

As a final point we note again that when a particle moves, its reconstructed image will move in sympathy. Because the backscatter PSF's have a cyclic phase variation in the axial direction, the phase of the reconstruction at a given point in space will change according to the movement of the surrounding particles in this direction. By measuring the rate of change of phase, or Doppler frequency, the axial velocity of the particles can be deduced. This is the basis of laser Doppler velocimetry that typically exploits a confocal configuration [38] and more recently has been exploited in Doppler OCT [5]. A good example of Doppler OCT showing retinal vasculature by Baumann et al. [37] is presented in Fig. 8.21.

The arterial and venous vessels in the papilla can be clearly distinguished. It is noted, however, that in Fig. 8.21a there appears to be bidirectional flow within the vessels. This is because the individual depth scans are obtained at a rate of 100 kHz which is insufficient to resolve the phase change unambiguously. By increasing the sample rate to 200 kHz the problem is resolved.

## 8.7 Conclusion and Discussion

This chapter has compared the 3D imaging methods DHM, OCT, CSI, and confocal microscopy with reference to their point spread and transfer characteristics. There is a major distinction between coherent microscopy, that records a single coherent image at a single wavelength, and the other, tomographic, techniques that construct an image from a range of wavelengths and illumination conditions. The tomographic techniques provide superior performance when compared to coherent microscopy but require additional images to be taken with different illumination conditions. This additional information comes at the expense of time and frequently it is necessary to compromise performance.

Although coherent microscopy can only be used to study relatively sparsely seeded flows, it is currently the only flow mapping technique capable of simultaneous whole-field flow measurement. Line transfer CCD cameras and double pulsed laser sources, that are often used in particle image velocimetry, make it possible to record pairs of holograms separated by 1–2 μs at megapixel resolution and at more than 1,000 frame pairs per second. For micro-flow measurement this means a maximum flow velocity of approximately 1–10 m/s depending on the configuration.

To image through scattering media or increase the data density by introducing more seeding particles it is necessary to use a tomographic technique. Doppler OCT is now used routinely, both to image and measure blood flow within the retina. In its original form OCT used a configuration similar to low NA CSI and used a broadband incoherent source. This configuration is referred to as space domain OCT and required slow mechanical scanning. Commercial swept-source OCT systems now exploit fast scanning laser sources to measure the backscattered light scattering along the path of a weakly focused beam. 2D scanning mirrors are required to produce a complete 3D image. Typically the depth scan rate is around 100–200 kHz, and this limits the maximum velocity to around

25–50 mm/s. Although, only the velocity component along the viewing direction is measured and this generally varies with position the 3D flow field can be synthesized from three or more data sets.

The methods of CSI and confocal microscopy have been included in this chapter because of their close relationship to the other techniques. As described in Section 3 both quasi-monochromatic CSI and confocal microscopy derive 3D information by illuminating the object with plane waves from different angles within the NA of the objective. Additionally, broadband CSI exploits spectral information like OCT. According to linear theory, CSI and confocal microscopy will work with more densely seeded flows than DHM and offer significantly better resolution than OCT.

Nevertheless OCT remains the method of choice for in vivo flow measurement for several reasons. Fundamentally, OCT is different from all the other methods. In DHM, CSI and confocal microscopy lateral and depth resolution are coupled as they are proportional to NA and the square of the NA, respectively. In OCT the depth resolution is proportional to the bandwidth of the source and this decoupling allows the PSF of OCT to be tailored to suit different scales. This is exploited in many examples of in vivo imaging since propagation through a rough distorting surface (e.g., the epidermis) generally ruins the fidelity of images with large NA. It is this flexibility, plus the efficiency of swept-source scanning that makes OCT such a powerful tool for biomedical applications.

## References

1. Abbe E (1874) A contribution to the theory of the microscope and the nature of microscopic vision. Proc Bristol Nat Soc 1:200–261
2. Zernike F (1942) Phase-contrast, a new method for microscopic observation of transparent objects. Part 1. Physica 9:686–698
3. Zernike F (1942) Phase-contrast, a new method for microscopic observation of transparent objects. Part II. Physica 9:974–986
4. Minsky M (1988) Memoir on inventing the confocal scanning microscope. Scanning 10:128–138
5. Fercher AF, Drexler W, Hitzenberger CK, Lasser T (2003) Optical coherence tomography—principles and applications. Rep Prog Phys 66:239
6. Garcia-Sucerquia J, Xu W, Jericho SK, Klages P, Jericho MH, Kreuzer HJ (2006) Digital in-line holographic microscopy. Appl Opt 45:836–850
7. Zhang T, Yamaguchi I (1998) Three dimensional microscopy with phase-shifting digital holography. Opt Lett 23:1221–1223
8. Cuche E, Marquet P, Depeursinge C (1999) Simultaneous amplitude-contrast and quantitative phase-contrast microscopy by numerical reconstruction of Fresnel off-axis holograms. Appl Opt 38:6994–7001
9. Kuehn J, Montfort F, Colomb T, Rappaz B, Moratal C, Pavillon N, Marquet P, Depeursinge C (2009) Submicrometer tomography of cells by multiple wavelength digital holographic microscopy in reflection. Opt Lett 34:653–655
10. Cuche E, Bevilaqua F, Depeursinge C (1999) Digital holography for quantitative phase-contrast imaging. Opt Lett 24:291–293
11. Lobera J, Coupland JM (2008) Contrast enhancing techniques in digital holographic microscopy. Meas Sci Technol 19:025501

12. Ferraro P, Wax A, Zalevsky Z (2010) Coherent light microscopy. Springer, Berlin
13. Huang D, Swanson EA, Lin CP, Schuman JS, Stinson WG, Chang W, Hee MR, Flotte T, Al E (1991) Optical coherence tomography. Science 254:1178–1181
14. Dresel T, Hausler G, Venzke H (1992) Three-dimensional sensing of rough surfaces by coherence radar. Appl Opt 31:919–925
15. Lee BS, Strand TC (1990) Profilometry with a coherence scanning microscope. Appl Opt 29:3784–3788
16. Schmitt JM (1999) Optical coherence tomography (OCT): a review. IEEE J Sel Top Quant Electron 5:1205
17. Bouma BE, Tearney GJ (2002) Handbook of optical coherence tomography. Marcel Dekker, New York
18. Drexler W, Fujimoto JG (2008) Optical coherence tomography: technology and applications. Proceedings of SPIE the international society for optical engineering, Springer
19. Brezinski M (2006) Optical coherence tomography: principles and applications. Academic, Burlington, MA
20. Lauer V (2002) New approach to optical diffraction tomography yielding a vector equation of diffraction tomography and a novel tomographic microscope. J Microsc 205:165–176
21. Coupland J, Lobera J (2008) Optical tomography and digital holography. Meas Sci Technol 19:070101. doi:10.1088/09570233/19/7/070101
22. Kak AC, Slaney M (1987) Principles of computerized tomography. IEEE, Piscataway, NJ
23. Wilson T (ed) (1990) Confocal microscopy. Academic, San Diego, CA
24. Leach R (2011) Optical measurement of surface topography. Springer, Berlin
25. Ruiz PD, Huntley JM, Coupland JM (2011) Depth-resolved imaging and displacement measurement techniques viewed as linear filtering operations. Exp Mech 51(4):453–465
26. Wolf E (1969) Three-dimensional structure determination of semi-transparent objects from holographic data. Opt Commun 1:153–156
27. Dandliker R, Weiss K (1970) Reconstruction of three-dimensional refractive index from scattered waves. Opt Commun 1:323–328
28. Born M, Wolf E, Bhatia AB (1999) Principles of optics. Cambridge University Press, Cambridge
29. Bragg WL (1913) The diffraction of short electromagnetic waves by a crystal. Proc Cambridge Philos Soc 17:43–57
30. Gabor D (1948) A new microscopic principle. Nature (London) 161:777–778
31. Gabor D (1949) Microscopy by reconstructed wavefronts. Proc Roy Soc Lond Ser A 197:454
32. Jericho MH, Kreuzer HJ (2010) Point source digital in-line holgraphic microscopy. In: Ferraro P, Wax A, Zalevsky Z (eds) Coherent light microscopy. Springer, Berlin, pp 3–30
33. Leith EN, Upatnieks J (1962) Reconstructed wavefronts and communication theory. J Opt Soc Am 52:1123–1130
34. Wormald SA, Coupland JM (2010) On measuring 3D flow within inkjet droplet streams using a digital holographic microscope. J Modern Opt 57(9):700
35. Alex A, Povazay B, Hofer B, Popov S, Glittenberg C, Binder S, Drexler W (2010) Multispectral in vivo three-dimensional optical coherence tomography of human skin. J Biomed Opt 15:026025
36. Coupland JM, Halliwell NA (1992) Particle image velocimetry: three-dimensional fluid velocity measurements using holographic recording and optical correlation. Appl Opt 31:1005–1007
37. Baumann B, Potsaid B, Kraus MF, Liu JJ, Huang D, Hornegger J, Cable AE, Duker JS, Fujimoto JG (2011) Total retinal blood flow measurement with ultrahigh speed swept source/Fourier domain OCT. Biomed Opt Exp 2:1539–1552
38. Durst F, Melling A, Whitelaw J (1981) Principles and practice of laser Doppler anemometry. Academic, London